DESIGN OF A SIX-AXIS AERODYNAMIC BALANCE FOR PHASE-LAG MEASUREMENTS ON TILT-MOUNTED HELICOPTER ROTORS

Pietro Li Volsi
Doctor, R&D Engineer
TIDAV SAS
Toulouse, France

Vivien Jourdon
Software Engineer
TIDAV SAS
Toulouse, France

Cédric Lefort
CEO
TIDAV SAS
Toulouse, France

ABSTRACT

This paper describes the design, development, and validation of an aerodynamic balance that uses a Stewart platform-based six-axis force/torque sensor. The main objective is to measure the forces and moments generated by the tilt-mounted helicopter rotor equipping the TIDAV T-H3 vertical take-off and landing (VTOL) drone. Additionally, it is crucial in measuring the previously observed 35° phase lag. Due to the 31" rotor diameter, stiff carbon fiber blades and absence of a flapping hinge, this value differs from the standard phase lags observed in conventional helicopter rotors, which typically range from 75° to 90°, depending on the hinge technology. The first part of the paper details the design process, the calibration of the six sensors, and the accuracy of the balance using a standard multicopter rotor. The balance is then used to measure the performance and the phase lag of the T-H3 tiltrotor.

NOTATION

*

Symbols

A_F Cyclic-induced force magnitude, N

A_M Cyclic-induced moment magnitude, N·m

c Chord, m

C_{l_α} Lift curve slope of the blade airfoil, -

f_i Force measured by the i-th leg, N

F_x Force in the x-axis, N

F_y Force in the y-axis, N

F_z Force in the z-axis, N

$\mathbf{F}_e$ Final force vector measured at the platform, N

$\mathbf{H}$ Transformation matrix, -

$k(\mathbf{H})$ Condition number of the matrix, -

I_b Blade inertia about flapping hinge, kg· m^2

$\overline{l_i}$ Mean length of the legs, m

$\hat{\mathbf{l}}_i$ Unitary leg vector, -

L_y Distance of rotor-balance along y-axis, m

M_x Moment in the x-axis, N·m

M_y Moment in the y-axis, N·m

M_z Moment in the z-axis, N·m

$\mathbf{M}_e$ Moment vector measured at the platform, N·m

r Maximum radius of the platform, m

R Maximum radius of the base, m

R_b Blade radius, m

α Blade pitch, degrees

γ Lock Number, -

θ Cyclic pitch magnitude, degrees

θ_0 Collective pitch angle, degrees

$\theta_{\mathbf{lon}}$ Longitudinal cyclic pitch, degrees

$\theta_{\mathbf{lat}}$ Lateral cyclic pitch, degrees

ρ Air density, kg/m^3

ϕ Cyclic phase angle, degrees

$\phi_{\mathbf{eff}}$ Effective cyclic pitch direction, degrees

ϕ_{0F} Phase lag of the force, degrees

ϕ_{0M} Phase lag of the moment, degrees

Ω Rotor speed, tr/min

*

Acronyms

VTOL Vertical Take-Off and Landing

BEMT Blade Element Momentum Theory

CoG Center of Gravity

INTRODUCTION

Force/torque sensors are essential tools for measuring the aerodynamic forces and moments created by lifting devices such as wings (Ref. 1), propellers (Ref. 2) and rotors (Ref. 3). The complex swashplate system present in the helicopter rotors generates aerodynamic forces and moments on the three axes, enabling the helicopter to rotate and move in all directions. This is achieved with the assistance of a tail rotor or a second contra-rotating rotor, which counteract the torque produced along the rotor's normal axis. Helicopters are thus able to vertically take-off/land, and perform hovering flight, which is critical for search-and-rescue and inspection missions. Measuring and predicting the rotor aerodynamic wrench is therefore crucial to understand the rotor dynamics and its impact on the helicopter overall dynamic performance, and most important for certification (Ref. 4). This understanding becomes even more pertinent with the advent of new aviation technologies.

The development of simple, cost-effective electric motors has led to the emergence of multicopter e-VTOL (electric vertical take-off and landing) aircrafts in recent years. This has resulted in the rise of numerous companies specializing in the design of e-VTOL aircraft with the intention of competing with established helicopters.

TIDAV T-H3 (shown in Figure 1) is a tiltrotor e-VTOL drone that combines the advantages of helicopters, multicopter e-VTOLs and aircrafts. It is composed of four fully tiltable wings (two at the front and two at the back) and two tiltrotors aligned with the lateral axis intersecting the center of gravity (CoG) of the drone. Similarly to the V-22 Osprey and the Agusta Westland AW609 TiltRotor, the T-H3 tiltrotors are equipped with swashplate systems that make the drone capable of vertical take-off and landing when the rotors are pointing upwards. Once they are tilted forward (towards the longitudinal axis of the drone), its dynamics switches to that of a fixed-wing aircraft, where the four wings are primarily responsible for supporting the drone weight. In this configuration, the rotors serve solely to counteract the drag experienced by the drone, thus enhancing the vehicle's endurance and range.

Compared to multicopters, helicopters and standard VTOLs, the main advantage of the T-H3 is the possibility to perform longitudinal and lateral flights without tilting the entire frame, avoiding therefore an increase in its frontal and lateral projected surfaces, respectively. When unexpected wind-generated aerodynamic pitching and rolling moments induce a rotation of the drone, the rotor cyclic swashplates play a key role in counteracting them. A cyclic input in the rotor swashplate results in a periodic change in the blade pitch, causing the blades to increase and decrease their lift coefficient as they rotate, enabling the control over the pitch and roll axes. This gives the drone unprecedented performance in the presence of strong wind gusts, allowing it to maintain a horizontal platform in critical phases such as take-off and landing.

Figure 1. TIDAV T-H3 VTOL drone.

To quickly identify the main strengths and weaknesses of this recently patented drone, off-the-shelf components were preferred to reduce time and prototyping costs to a minimum. The tiltrotor system studied in this paper is composed of a T-Motor motor and a three-bladed Align swashplate system. The rotor blades were originally part of a 26" T-Motor Multicopter two-bladed rotor, and they have been mounted on the swashplate system without flapping hinge, resulting in a final rotor diameter of 31". Preliminary calculations using standard Blade Element Momentum Theory (BEMT) and beam theory have permitted to calculate the Lock number (Ref. 5), which defines the ratio of the aerodynamic to the inertial forces:

$$\gamma = \frac{\rho \ c \ C_{L\alpha} \ R_b^4}{I_\beta} = 12.6 \tag{1}$$

In Eq. 1, ρ represents the air density, c is the mean chord of the blade, $C_{L\alpha}$ is the aerodynamic 2D lift slope of 2D the airfoil used in the blade, R_b is the blade radius and I_b is the moment of inertia around the flapping hinge.

While this dimensionless number varies generally from 5 to 10 (Ref. 3) for standard helicopter rotors, it may be lower for rotors designed to fly on Mars (in (Ref. 6), the measured rotor Lock number was 4 on Earth atmosphere and 0.33 in Mars conditions), and higher for stiffer and/or hingeless rotors like the one equipping the T-H3 (Ref. 3).

As rotor blades can be assimilated to rotating mass-spring systems around their flapping hinge (which can be either real or virtual in the case of hingeless rotors), a periodic forcing input induces an output with the same frequency and a phase lag. In the case of an articulated rotor with a central flapping hinge, the rotor experiences a phase lag of 90°. However, for hingeless rotors or rotors with stiff flapping hinges, the phase lag is lower than 90°. According to Leishman (Ref. 3), this can reach 75°-80° on standard helicopter, or can be as low as 30°- 40° as discussed by Halley (Ref. 7). Preliminary on ground tests on the T-H3 actual rotor configuration revealed a 35° phase lag, which is more in line with Halley's values.

The objective of the present paper is to experimentally measure the phase lag through an aerodynamic six-axis force/torque sensor subject to different operational and manufacturing constraints. For this, an in-house force/torque sensor has been created. It is described, calibrated and validated in the following section, and then used to evaluate the performance and the rotor phase lag.

FORCE/TORQUE SENSOR DESIGN

Six-axis balances are capable of measuring the forces and moments relative to a fixed three-dimensional Cartesian coordinate system. As the airflow around the aircraft generates forces and moments around the aircraft axes, these sensors are used in wind tunnels to evaluate the forces/moments generated at the center of gravity (CoG) of the aircraft (see Fig. 2), and to validate the aerodynamic performance predicted during the design phase. By changing the angle-of-attack and sideslip of the aircraft relative to the wind, the aerodynamic polars and flight envelope of the aircraft are computed. Similarly, the performance of drone propellers and helicopter rotors are assessed using multi-component force/torque sensors. Fig. 2 shows an example of a test-rig using a six-axis aerodynamic balance to measure the aerodynamic forces and moments generated by the drone propeller.

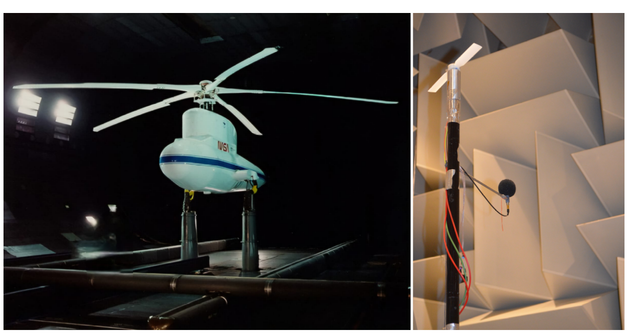

Figure 2. On the left: Sikorsky bearingless rotor mounted in 40- by 80-Foot Wind Tunnel (Ref. 8) (Credits: NASA); on the right: ISAE-SUPAERO experimental setup showing the rotor, the motor and the six-axis balance (Ref. 2) (Credits: ISAE-SUPAERO).

To ensure the veracity of the results, it is essential that the installations do not interfere unduly with the aerodynamic measurements. For this reason, the supports connecting the aircraft models and rotors to the balance must be streamlined to avoid any separation and additional drag that could affect the measurements.

As introduced in the previous section, the aim of this work is to develop a six-axis aerodynamic balance able to measure the forces and moments generated by the T-H3 tiltrotor. The operational constraints imposed upon the design of the present aerodynamic balance are the following:

- The balance must be able to measure the forces and moments generated by the tiltrotor on the three axes of the reference Cartesian coordinate system. This enhances the measurements of the hovering performance and handling qualities;
- The tiltrotor assembly must be easily attachable/detachable to the balance, to maintain the same configuration between the T-H3 tiltrotor and the one used in this work;
- The balance must interfere as little as possible with the rotor wake.

Given the weight of the drone, which ranges from 15 to 25 kg, and the positioning of the rotor center at a distance of 25 cm from the center of gravity, the balance must be capable of measuring forces of up to 300 N in the vertical z-axis and moments of up to 150 N·m in the x-axis. Especially these last constraints make commercial six-axis balances unsuitable. This section is therefore devoted to the design process that has led to the final in-house force/torque sensor.

Geometrical definition & optimization

Multi-component balances are designed to measure the deformation of simple elements, such as plates or beams, to determine the forces and moments that are applied to them by external devices. These systems consist of multiple load cells equipped with strain gauges that detect deformations. By utilizing specific electrical circuits, such as Wheatstone bridges, load cells can proportionally convert the amplitude of deformation into changes in electrical resistance or voltage (Ref. 1). By arranging multiple load cells, it is possible to measure deformations at various points and along arbitrary axes. In an aerodynamic six-axis balance, the forces recorded by six load cells can be reduced to a three dimensional mechanical wrench calculated at the aircraft center of gravity and along the aircraft main axes. The goal of this work is to measure the forces and moments generated by the helicopter-type rotor equipping the T-H3 drone.

The geometry of the present balance is inspired by the Stewart Platform (Ref. 9). Created by Stewart in 1965, it is composed of six extendable and retractable legs connecting the base plate to the platform and is used to simulate the aircraft (or car) rotations and translations. Thanks to its simplicity, it has become an essential tool to train helicopter/aircraft pilots, and sports car racing drivers.

In the balance, the legs rigidly connect the base plate to the platform plate, where the forces and moments are applied and measured using the six load cells embedded in the legs. The geometrical definition of the six axis balance is shown in Fig. 3, which corresponds to that used by Dwarakanath *et al.* (Ref. 10).

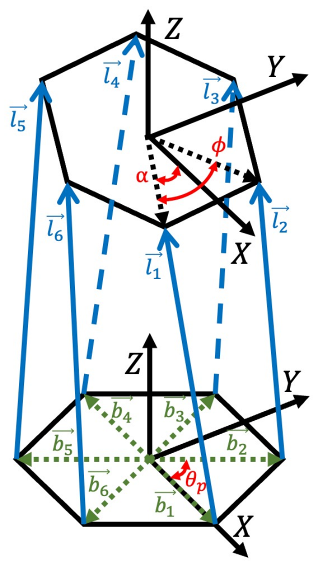

Figure 3. The geometrical definition of the Stewart platform based balance.

The forces and moments on the three axes (X, Y, Z) are calculated using Eq. 2, provided that the whole balance is stiff enough:

$$\begin{cases} \sum_{i=1}^{6} \hat{\mathbf{l}}_i f_i = \mathbf{F}_e \\ \sum_{i=1}^{6} \mathbf{b}_i \times \hat{\mathbf{l}}_i f_i = \mathbf{M}_e \end{cases} \Rightarrow \begin{Bmatrix} \mathbf{F}_e \\ \mathbf{M}_e \end{Bmatrix} = \mathbf{H}\{\mathbf{F}\} \tag{2}$$

Where:

- i refers to the legs;
- $\hat{\mathbf{l}}_i$ is the unitary leg vector;
- $\mathbf{b}_i$ represents the position vector of the i-th point of the base plate (respect to the base center);
- f_i is the force measured by the i-th leg;
- $\mathbf{H}$ is the transformation matrix;
- $\mathbf{F}_e$ and $\mathbf{M}_e$ are the final force and moment vector measured at the platform, respectively.

To avoid a singular and hill-conditioned $\mathbf{H}$ matrix, which could potentially lead to inaccurate results, a numerical optimization was used to determine the geometry of the balance, where the condition number of the matrix was minimized: $k(\mathbf{H}) = \|\mathbf{H}\| \cdot \|\mathbf{H}^{-1}\|$. To reduce the distance between the rotor and the center of the platform, the maximum radii of both platform (noted R) and base (noted r) allowed to the optimization algorithm were fixed to 0.13 m. Additionally, the length of the legs was fixed to 0.075 m because of the 15 kg off-the-shelf load cells initially used. The optimization parameters and constraints are summarized in the following table:

Objective		$\min(k(\mathbf{H}))$
Parameter	**Min**	**Max**
r [m]	0.10	0.13
R [m]	0.10	0.13
α [°]	0.0	60.0
ϕ [°]	5.0	60.0
θ [°]	5.0	60.0
Constraints		**Value**
$\overline{l_i} = \frac{1}{6}\sum_{i=1}^{6} l_i$ [m]		0.075
$\sqrt{\frac{1}{6}\sum_{i=1}^{6}(l_i - \overline{l_i})^2}$ [m]		0.0

Table 1. Optimization objective, parameters and constraints.

The optimization slightly differed from the one performed by Dwarakanath *et al.* (Ref. 10). In the present work, to reduce the development costs to a minimum, the length of all legs was fixed to 0.075 m, while Dwarakanath *et al.* (Ref. 10) allowed the optimization to change the height of the platform, leading to different lengths of the legs (three-by-three). To do so, the height of the balance was adapted so that the mean value of all the legs corresponded to the constraint value. The three angles were also adapted to ensure that all the legs had exactly the same length. This was set up in the optimization imposing an additional constraint on the standard deviation of the legs lengths. The optimization framework Pymoo (Ref. 11) coded in Python (Ref. 12) and its Genetic Algorithm were used, with a population of 500 candidates per generation and a total of 50 generations. Both crossover and mutation were activated, with 90% probability of crossover and 10% on the mutation. The resulting matrix condition number was 11.02, with the final geometry shown in Fig. 4.

To guarantee the stiffness of the balance, 4 different carbon plates (3 mm thick) were used (see Fig. 5). Two on the platform and two on the base, connected by multiple hexagonal standoffs to rigidify the assembly. The balance was designed to accommodate the T-H3 native tiltrotor along its y-axis.

Because 15 kg load cells were not sufficient to fully evaluate the performance of the rotor in hovering conditions at thrust levels higher than 100 N, DYLY 106 50 kg load cells were chosen. As they slightly differed in length, the height of the already manufactured balance was adapted to accommodate the 0.084 m legs, resulting in a final condition number of 14.01.

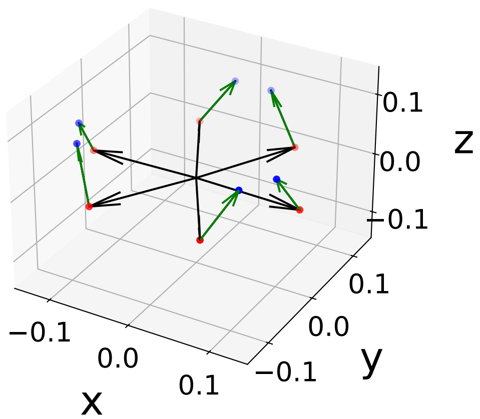

Figure 4. Optimized balance configuration. Red and green points belong to the base and platform, respectively. The green arrows correspond to the leg vectors and the black arrows to the position vectors of the base plate.

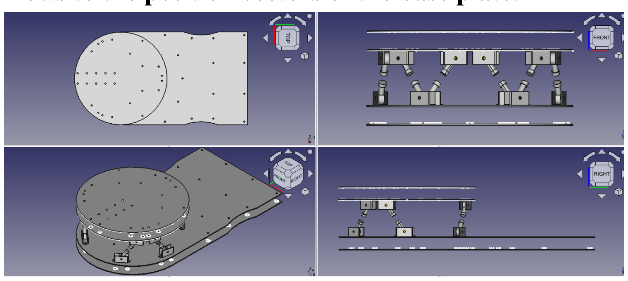

Figure 5. CAD model of the final six-axis aerodynamic balance. The software used to create the CAD model was FreeCAD.

Sensors & balance calibration

As introduced in the previous subsection, load cells convert the deformations measured by strain gauges into a variation of the electrical resistance of a Wheatstone electrical bridge. Before implementing the six load cells on the balance, it was mandatory to calibrate them and evaluate their accuracy. To achieve this, they were suspended, and different calibration weights were attached on them. The measurements were performed using a HX711 force amplifier connecting the DYLY 106 50 kg load cells to an Arduino MEGA. The whole system had a sampling frequency of 20 Hz, which was enough to measure stationary loads. The values registered by the Arduino were averaged over 10 seconds to find the coefficients (a,b) of the fitted linear equation $y = a \cdot x + b$. x represents the calibrated weight and y the output of the sensor. The calibration was performed on both tension and compression (the setups are shown in Fig. 6), through three different sets of loads/unloads.

Fig. 7 shows the measures and the errors of the leg N°1. The errors measured on the other legs (shown in the appendix) were generally lower than 1 %.

The load cells were then placed along the balance legs and

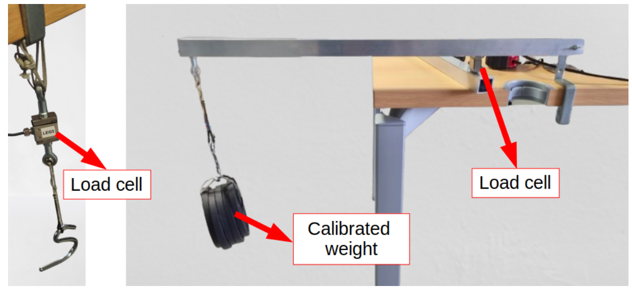

Figure 6. Tension (on the left) and compression (on the right) calibration setups.

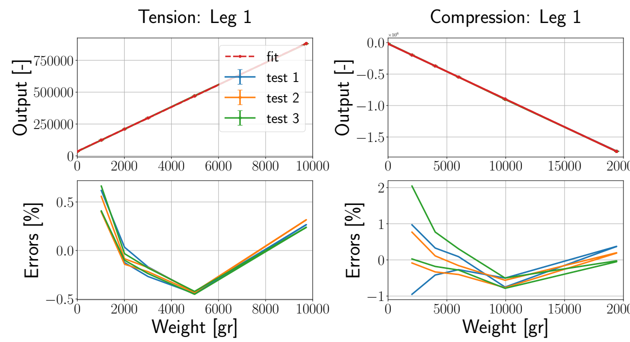

Figure 7. Tension (on the left) and compression (on the right) calibration results. On top the outputs of the balance are plotted vs. the calibrated weight. On the bottom, the errors vs. the calibrated weight.

were connected to the platform and base plates using ball joints on both ends to ensure that the load cells only worked in tension or compression. The final matrix **H** was verified using the same calibration weights. To determine the accuracy of the matrix, the balance was inclined along the x and y axes, a support beam was added in $-y$ direction to develop a torque along different axes and the calibration weights were added. Three loading/unloading sets per balance configuration were performed, and the 10 seconds averaged final values were compared to the theoretical values. Five different tests (some of which shown in Fig. 8) were carried out:

1. The weights were positioned at the center of the balance. Only F_z was excited.
2. The weights were suspended at $y = 36.25$ cm while the balance was horizontal. Only F_z and M_x were excited;
3. Same setup as Test 2, but the test-stand was rotated by 45° along the x-axis. F_y, F_z, M_x were excited;
4. Same setup as Test 2, but the balance was rotated by 45° along the y-axis. F_x, F_z, M_x, M_y and M_z were excited;
5. Same setup as Test 2, but an additional support beam was added along the x direction, so that the calibration weights were suspended at a distance $x = -39.2$ cm. This excited F_z, M_y, M_x.

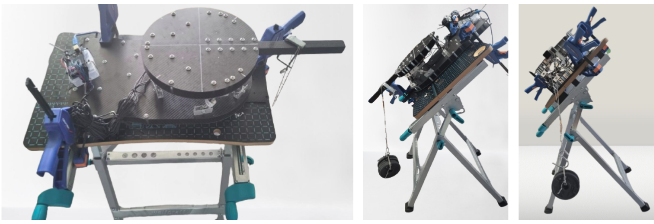

Figure 8. Three different tests performed to verify the matrix H. From left to right: Tests 2, Test 3 and Test 4.

The results presented in the Appendix show errors reaching up to 20% (on only three tests) when the calibrated weights were less than 2 kg. For weights above this value, the errors decreased, generally remaining below 5%. These differences may be due to multiple reasons. The matrix **H** may not accurately represent the real balance geometry. This is demonstrated by the non-zero values measured by the balance along the non-excited axes by the test. Also, the rotation along the X and Y axis in test 3 and 4, manually measured with an inclinometer, may lack sufficient precision. To improve this aspect, a calibration process using a robotic arm and a deep neural network model as used by Seok Oh *et al.* (Ref. 13) could be employed. This may improve the accuracy of the balance. Due to an imperfectly conditioned matrix, small variations in the forces measured by the legs may result in significant variations in the mechanical wrench. In this case, a new optimization could be performed to ensure a good conditioning of the matrix H with the 50 kg load cells.

Test on 26" T-Motor rotor

Before implementing the T-H3 native tiltrotor on the balance and measuring the phase lag, the two-bladed 26" T-Motor G26 rotor was tested. This rotor presented the same blades as the T-H3 tiltrotor. To automatize the tests, the rotor was controlled via a Holybro Pixhawk 5X flight controller module and the PX4 autopilot and connected to the 3 kW Mean Well RSP-3000-48 power supply. Both MN1010 KV135 T-Motor and the ESC Flipsky FSESC75100 were mounted on a carbon fiber support beam connected to the y-axis of the platform. The rotor center was located at a distance of $y = 50$ cm from the platform center to avoid any interaction between the rotor wake and the balance. This setup is shown in Fig. 9.

To analyze the reliability and repeatability of the results under different conditions, two distinct rotors were employed: one clockwise (CW) rotor and another counter-clockwise (CCW). The two rotors were tested in a push-down (PD) and push-up (PU) configuration, resulting in a total of four tests.

A 15-second calibration of the balance with the motor at rest was performed before the beginning of each test. Next, the motor speed was increased from 2000 rpm to 4500 rpm and decreased back to 2000 rpm. The measurements were taken at 250 rpm intervals, which each measurement lasting for 10 seconds. The 8-second averages started 1.5 seconds following the increase (or decrease) of the rotational speed. The motor required 0.3 seconds to reach the new rotational speed.

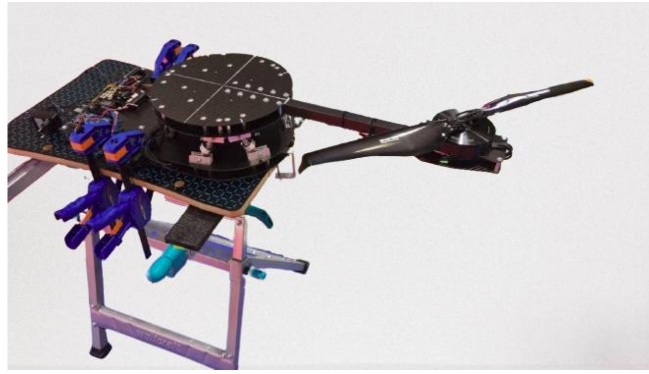

Figure 9. Setup used to evaluate the 26" T-Motor rotor.

Fig. 10 illustrates the rotor performance. The thrust F_z measured for all the configuration did not change across the different tests, meaning that, for push up or push down configurations, the measured thrust levels were reproducible (and repeatable, as each test was performed three times), although the difference between the reference data (published by the manufacturer) and the measurements show differences going up to 20% at 4500 rpm. The torque plot demonstrates bigger differences between the configurations, with the counter-clockwise rotor exhibiting values closer to the T-motor torque curve. As the electrical power curve measured with the assistance of an electrical current probe and a voltmeter matches the reference data, the final efficiency curves (denoted η) do not mirror the T-motor data, showing discrepancies reaching 1 gr/W at 4500 rpm and higher values at slower motor speeds. Variations in experiments on different specimens of a given rotor geometry may lead to discrepancies of up to 10%, as previously highlighted by Deters *et al.* (Ref. 14) in studies on small scale commercial rotors. However, the differences here measured are approximately 20% on both thrust and torque, and higher for low speed motor regimes. As pointed out in the previous subsection, the matrix **H** may be slightly off from the one representing the actual balance geometry. Nevertheless, the balance demonstrated consistent trends, providing confidence in the phase lag measurements presented in the subsequent subsection.

PHASE LAG EXPERIMENTAL STUDY IN STANDARD HOVERING CONDITIONS

As previously introduced, the aim of the present balance is to measure the phase lag experienced by the T-H3 tiltrotor. As this rotor is made up of three unhinged stiff carbon fiber blades, it has an estimated Lock number of 12. The higher this dimensionless number is, the higher are the aerodynamic forces respect to the inertial ones. Standard helicopter rotors presenting flexible blades and flapping hinge at their blade root generally present lower Lock numbers (from 8 to 10), with a consequent phase lag spanning from 90° (for fully articulated rotors) to 75° (for stiffer flapping hinges and rotor blades). In the case of the T-H3 tiltrotor, the phase lag

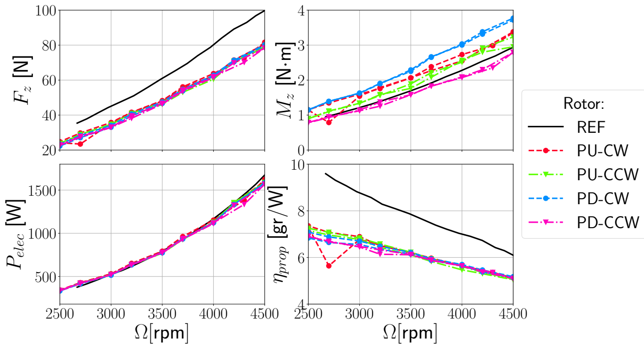

Figure 10. Performance comparisons between T-motor data and performance measured with present six-axis balance. The thrust (top-left), torque (top-right), the electrical power (bottom-left) and the efficiency (bottom-right) are showed as function of the rotational speed.

experienced by the drone was approximately 35°. In this section, the experiments leading to the measurement of the rotor phase lag are presented.

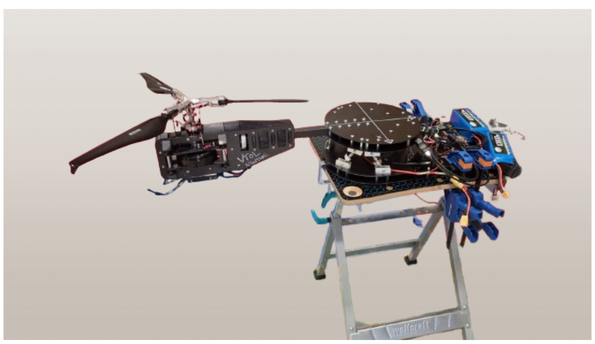

Figure 11. Setup of the balance used to perform the phase lag measurements on the T-H3 tiltrotor.

To perform the experimental tests, the support beam of the standard T-H3 tiltrotor was introduced along the y-axis of the balance and fixed in the allocated space (see Fig. 11). Apart from the tiltrotor, whose rotor center was located at a distance of $L_y = -0.525$ m from the center of the balance platform, the setup was the same as that used to measure the hovering performance of the T-Motor G26 rotor. In this case, the PX4 autopilot was used to control the motor speed (which was held constant at $\Omega = 3500$ rpm) via the ESC Flipsky FSESC75100. Additionally, it managed the collective and cyclic pitch angles of the rotor using the three-bladed ALIGN swashplate. The collective pitch (here noted θ_0) is used to change the pitch (here noted α) of all the blades axisimmetrically, modifying the thrust F_z and torque M_z produced by the rotor. The cyclic pitch modifies the pitch of the blade azimuthally at the motor speed frequency, reducing it on a hemicycle, and increasing it on opposite half of the disk. To control the cyclic pitch, two inputs are needed: the amplitude of the cyclic pitch (θ_{cyc}), and its direction defined by a unitary vector belonging to the XY plane of the balance and oriented with respect to the X axis by a cyclic phase angle ϕ_{cyc}. While the amplitude gives the maximum variation of the cyclic pitch, the direction permits to change the azimuthal distribution of the pitch variation. Both θ_{cyc} and ϕ_{cyc} are decomposed in the PX4 autopilot in a longitudinal component θ_{lon} and a lateral component θ_{lat} through Eq. 3:

$$\begin{cases} \phi_{cyc} = \arctan\left(\dfrac{\theta_{lat}}{\theta_{lon}}\right) \\ \theta_{cyc} = \sqrt{\theta_{lon}^2 + \theta_{lat}^2} \end{cases} \tag{3}$$

Fig. 12 shows two different examples, assuming that there is no phase lag (as the aim is to calculate it). A pure longitudinal cyclic $\theta_{lon} = 5°$, corresponding to the $\vec{x}$ longitudinal vector, is translated into a decrease of the blade pitch in the hemicycle on which the vector points, and an increase in the opposite side. In this case, the thrust difference between one hemicycle and the other produced by the difference in the blade pitch would lead the rotor to rotate around the Y-axis and, consequently, to move along the X-axis. On the contrary, if a pure Y-cyclic is applied, the left hemicycle experiences a decrease in the cyclic pitch, and the right hemicycle an increase of it, resulting in a rotation around -X and a translation along Y.

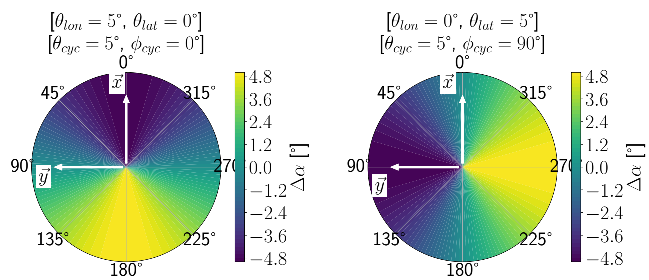

Figure 12. Two examples of azimuthal pitch variations of the blade for two different cyclic orientations: a longitudinal cyclic on the left and a lateral cyclic on the right.

Two different studies are presented in the following subsections. After having measured the phase lag for a given set of fixed parameters $\{\Omega = 3500$ rpm, $\theta_0 = -2°$, $\theta_{cyc} = 1.2°\}$, the cyclic pitch magnitude is modified to analyze the influence of this parameter on both the mechanical wrench and the phase lag.

Tiltrotor phase lag measurement

The objective of this subsection is to analyze the influence of the cyclic pitch phase ϕ_{cyc} on the mechanical wrench measured by the six-axis aerodynamic balance, to estimate the phase lag (noted ϕ_0). In the presence of a phase lag, the effective cyclic pitch direction (ϕ_{eff}) is rotated by the phase lag angle ($\phi_{\text{eff}} = \phi_0 + \phi_{\text{cyc}}$), in the direction of the rotor rotation. For the present counter-clockwise rotating T-H3 tiltrotor studied here, when a longitudinal cyclic pitch is applied, the effective rotation and movement of the rotor will be rotated counter-clockwise by the phase lag angle ϕ_0. It is therefore important to measure the forces and moments on the X and Y axes for different cyclic pitch phase ϕ_{cyc}, at a constant cyclic pitch magnitude θ_{cyc}. To do so, the cyclic pitch phase ϕ_{cyc} was modified from -180° to +180°. To avoid a hysteresis build-up by directly incrementing ϕ_{cyc} from -180° to 180°, two measures with no cyclic inputs ($\theta_{\text{cyc}} = 0°$) were taken before and after each cyclic variation and their averaged value was subtracted from the measurement where the cyclic pitch input ($\theta_{\text{cyc}} \neq 0°$) was applied. Furthermore, before increasing ϕ_{cyc} by 15° (for two tests, 10° for the third), a measurement on the opposite cyclic pitch direction was performed (see Fig. 13). This allowed to avoid any offset due to the hysteresis and analyze the effect of the cyclic pitch change on the mechanical wrench.

Since the rotor center did not coincide with the center of the balance platform, an additional moment, $F_z \cdot L_y$, was measured in M_x. To avoid any fluctuation in M_x due to the variations in the vertical force F_z, this induced moment was subtracted from M_x, ensuring that only the influence of the cyclic pitch was visible. Each cyclic input lasted for 5 seconds, and the measurements were averaged over 3 seconds, starting 1.5 seconds after the cyclic input change. For clarity and conciseness, only the variations in forces and moments in the X and Y axes are presented, as it was observed that the cyclic pitch variation had no significant effect on the rotor's thrust and torque. It is worth noting that the thrust generated by the rotor under the conditions $\Omega = 3500$ rpm, $\theta_0 = -2°$ is 6.3 kg.

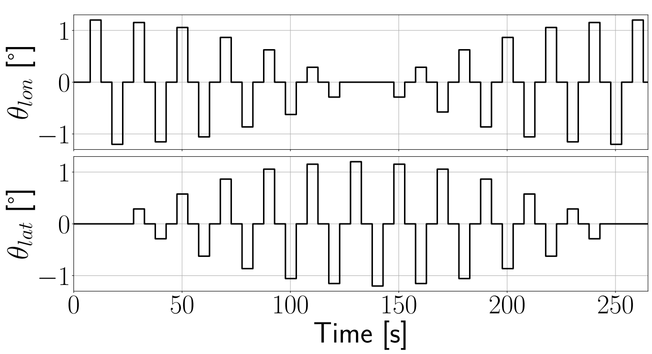

Figure 13. Time variation of longitudinal θ_{lon} and lateral θ_{lat} cyclic pitch used to measure T-H3 tiltrotor phase lag.

Fig. 14 shows the forces F_x and F_y and the moments M_x and M_y as function of the cyclic pitch phase ϕ_{cyc}. When comparing both M_x and M_y moments, both maximum moment amplitudes reached peaks of ~ 1.5 N·m (M_y reaching a slightly higher peak), with both curves resulting centered at 0 N·m. These moments around the X and Y axes may induce the disk actuator to rotate around these axes. In the T-H3 tiltrotor, the system composed of the rotor, swashplate, motor and ESC is connected to the tilt mechanism through 4 silent blocks used to absorb the motor vibrations. Since the silent blocks can deform, the thrust vector, which is normally parallel to the Z-axis of the balance, may develop components in the Y and/or X axes, thereby inducing forces F_y and F_x, respectively. Because the silent-blocks are squarely disposed around the plate fixed to the motor, the amplitudes of both F_x and F_y should be similar. However, it may be visible in the results that the maximum peak reached in the X axis is approximately twice the maximum force in the Y direction (3.0 N vs. 1.4 N). Even though the tilting system has a position set-point, a backlash may induce a small rotation around the Y-axis, leading to a stronger force component in the X-axis.

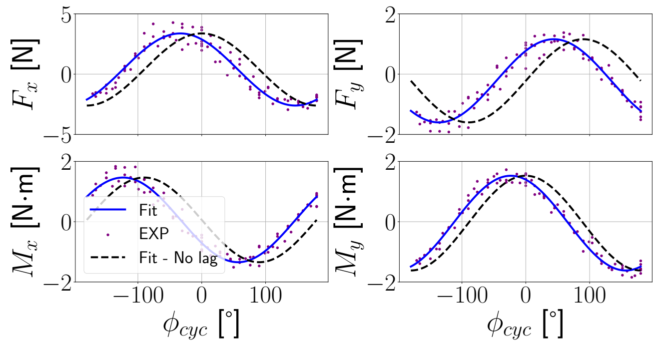

Figure 14. Forces (F_x and F_y) and moments (M_x and M_y) as function of the cyclic phase ϕ_{cyc}. Dots represent the average values, the solid curves represent the sinusoidal (for F_y and M_x) and cosinusoidal (for F_x and M_y) fitted curves. The ideal cyclic response curves with no phase lag are plotted for comparison.

To identify the phase lag ϕ_0, sinusoidal curves $A\sin(\phi_{\text{cyc}} + \phi_0)$ were fitted to F_y and M_x, while cosinusoidal curves $A\cos(\phi_{\text{cyc}} + \phi_0)$ were fitted to the F_x and M_y curves. Table 2 shows the parameters for the measured forces and moment fitted curves. The coefficients of determinations R^2 were all close to 1, meaning that the fitted curves well represented the experimental results. Table 2 shows also the phase lag angles measured for all forces and moments on both X and Y components. While F_x and M_x showed a phase lag value of 33°, the Y components of both forces and moments show different phase lag between themselves and F_x/M_x. On the one hand the averaged phase lag for the X and Y force components is 39.83°, which is approximately 5° off the initially observed value. On the other hand, the average of the phase lag measured on the moments is 28.35°, almost 7° lower than the 35° observed phase lag. These differences in the phase lag measurements may be due to the previously introduced non-perfect **H** matrix representation of the real six-axis aerodynamic balance. A balance with a more optimized geometry would probably lead to more accurate measurements of the phase lag.

Cyclic pitch magnitude influence on phase lag

Following the calculation of the phase lag of the T-H3 tiltrotor for a specified cyclic pitch $\theta_{\text{cyc}} = 1.2°$, two additional

Parameter	A	ϕ_0	R^2
F_x	2.99 N	33.48°	0.93
F_y	1.38 N	46.18°	0.94
M_x	-1.40 N·m	33.20°	0.96
M_y	1.57 N·m	23.50°	0.98

Table 2. Fitted Curve Parameters

tests at distinct cyclic pitch magnitudes $\theta_{\text{cyc}} = [2.4, 3.8]°$ were conducted to assess the impact of the cyclic pitch magnitude θ_{cyc} on the amplitude of the generated forces (A_F) and moments (A_M), as well as their phase lags (ϕ_{0F} and ϕ_{0M}, respectively). For each test, the same protocol previously described and shown in Fig. 13 was used. The cosinusoidal and sinusoidal curves were fitted to the new forces and moments and the parameters (the magnitude of the forces/moments A and the phase lag ϕ_0) are plotted in Fig. 15. Additional null points at $\theta_{\text{cyc}} = 0°$ were also included to facilitate the examination of the trends in force and moment amplitudes. Here are the principal findings:

- Both forces F_x and F_y demonstrated a linear trend, with the ratio F_x/F_y exhibiting an averaged factor of 1.86, which corroborates the observation described in the previous subsection. While the phase lag of the two force components differed for all cyclic pitch inputs, their difference reduces from 13° to approximately 3°, with an average getting closer to 34°;
- The moments showed a linear trend with no difference in the amplitude between M_x and M_y. In the phase lag curve, a slight decrease was observed in both the M_x and M_y phase lag curves, with an average of $\sim 21°$ for $\phi_0(M_y)$ and $\sim 27°$ for $\phi_0(M_x)$.

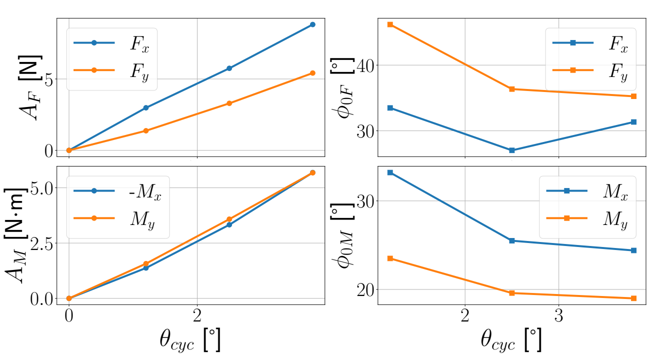

Figure 15. On the left: Magnitude of the forces (A_F, top) and moments (A_M, bottom) as function of the cyclic pitch magnitude θ_{cyc}. On the right: Phase lag measurements for the forces (ϕ_{0F}, top) and moments (ϕ_{0M}, bottom) as function of the cyclic pitch magnitude θ_{cyc}.

The 35° phase lag previously observed are therefore coherent with the phase lag measured by the balance on the forces. However, the moments show smaller phase lag and need a deeper analysis. These measurements are mitigated by the fact that errors may be induced by the non perfectly conditioned matrix H used to convert the forces into the mechanical wrench generated by the rotor, which can be corrected in the future by performing a recalibration of the balance using more sophisticated and accurate methods.

CONCLUSION & FUTURE WORK

In this work, the design, calibration, and validation of an in-house six-axis aerodynamic balance based on the Stewart platform and developed to measure the aerodynamic forces and moments generated by the T-H3 tiltrotor e-VTOL drone were presented. The balance design was optimized to ensure minimal interference with the rotor wake while providing force and torque measurements on the three axes and under various operational constraints. The manufactured balance was capable of measuring forces up to 300 N and moments up to 150 N·m, making it suitable for evaluating the performance of the T-H3's tiltrotor system (which was designed to push up to 150 N in hover).

The calibration process demonstrated that the six load cells used in the balance had an accuracy within 1% error. When mounted in the balance, errors increased up to 20% when the applied loads were below 2 kg and 5% above, which may be attributed to slight deviations in the balance geometry and the non-perfect conditioning of the matrix **H** needed to convert the load cells forces into the final mechanical wrench.

After the calibration of the load cells and the balance, experimental tests conducted on a 26" commercial rotor verified the capability of the balance to measure the aerodynamic performance, despite showing a discrepancy of approximately 20% in thrust and torque measurements compared to reference data published by the rotor manufacturer. However, the capability of measuring the good trends provided confidence in the balance's ability to measure T-H3 tiltrotor phase lag.

The primary objective of this study was to measure the phase lag of the T-H3 tiltrotor, characterized by its stiff, unhinged blades with an estimated Lock number of 12. The experiments performed by varying the cyclic pitch phase from -180° to +180° revealed a phase lag of approximately 38° to 34° on the forces, consistent with empirical observations. However, the phase lag measured on the moments show smaller values and need some deeper analyses. The phase lag remained relatively constant across different cyclic pitch magnitudes, while the amplitudes of the forces and moments varied linearly with the cyclic pitch magnitude.

Overall, the developed six-axis aerodynamic balance proved to be an effective tool for evaluating the performance and dynamic characteristics of the T-H3 tiltrotor. The results obtained from this study provided valuable insights into the rotor dynamics, essential for optimizing the performance and control system of the T-H3 e-VTOL. Future work may focus on refining the balance design to reduce measurement errors and test the influence of the collective pitch and the rotational speed to the phase lag. Furthermore, tests will be performed with the tiltrotor submitted to an oncoming flow generated by a commercial multi-fan wind generator, in order to analyze the phase lag in conditions closer to the transition phase.

Author contact: Pietro Li Volsi, pietro.li-volsi@tidav.aero Vivien Jourdon, vivien.jourdon@tidav.aero Cédric Lefort, cedric.lefort@tidav.aero

APPENDIX

Load cell calibrations

The load cell calibration curves are presented in Table 3:

Calibration

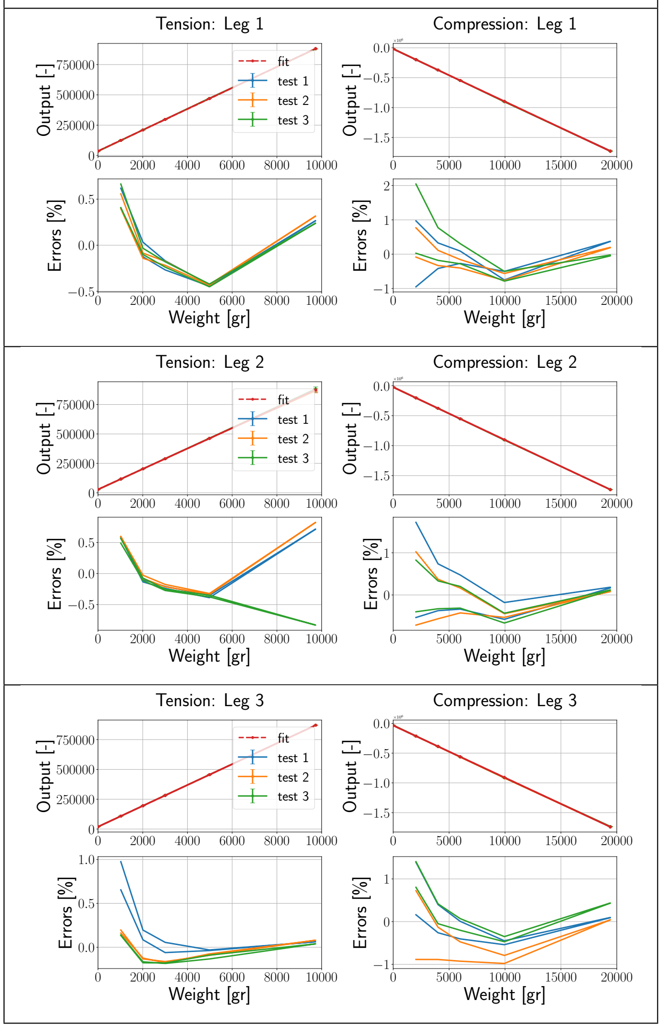

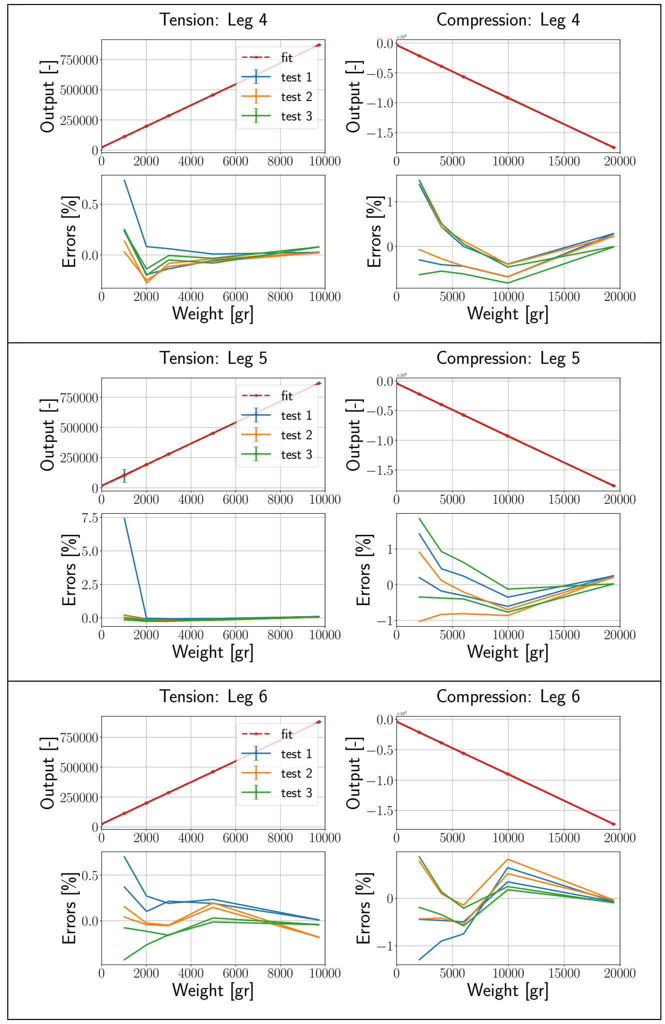

Table 3. Tension and compression tests used to calibrate the load cells.

Balance calibration

The balance calibrations are presented in the following table, allowing for the evaluation of accuracy across the six different axes. As observed, even the axes not excited by the calibration weights may show non-zero measurements. For these axes, errors are not calculated, and zeros are displayed in Table 4.

Test 1

Calibration values

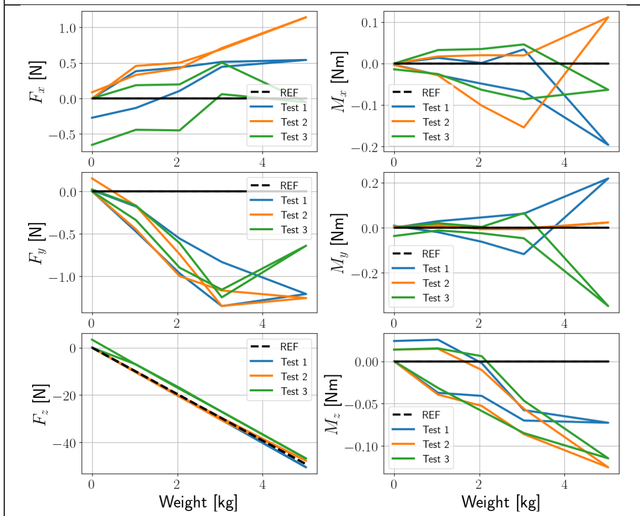

Errors

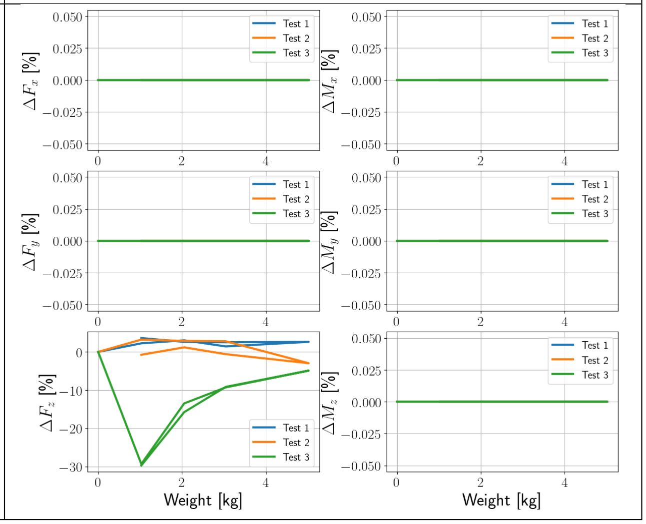

Test 2

Calibration values

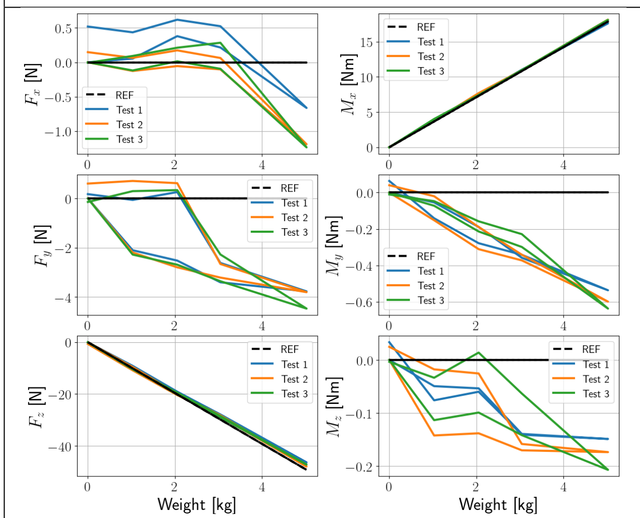

Errors

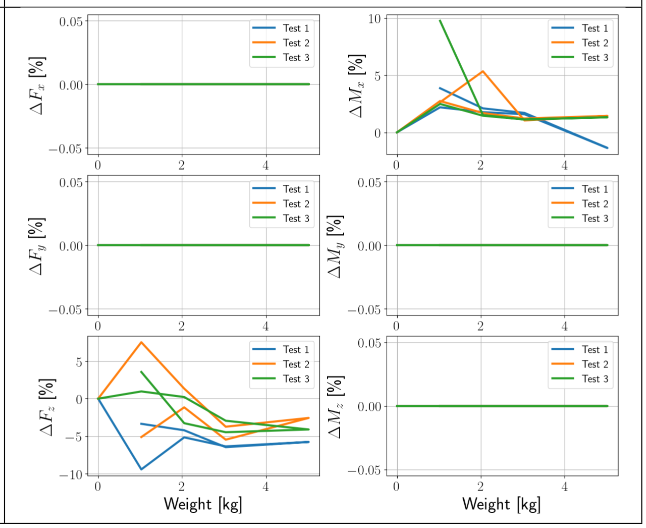

Test 3

Calibration values

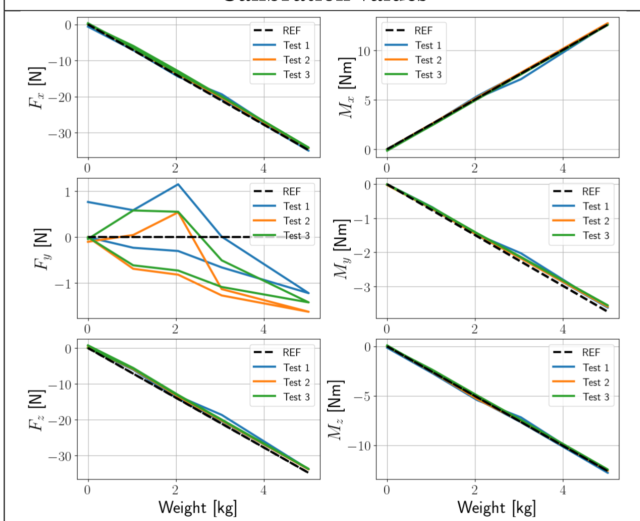

Errors

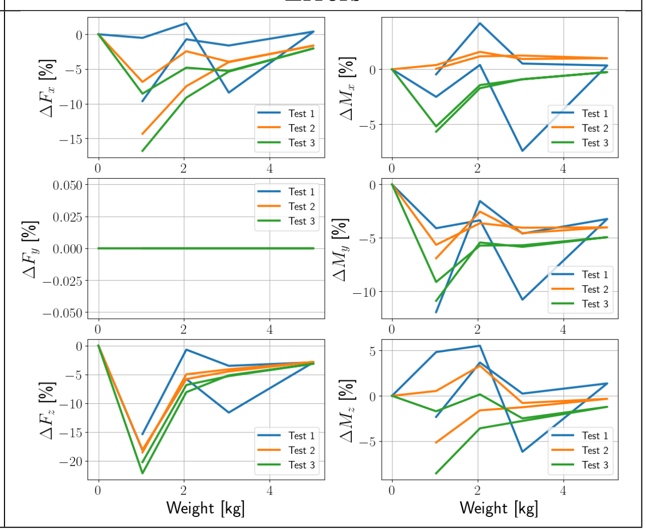

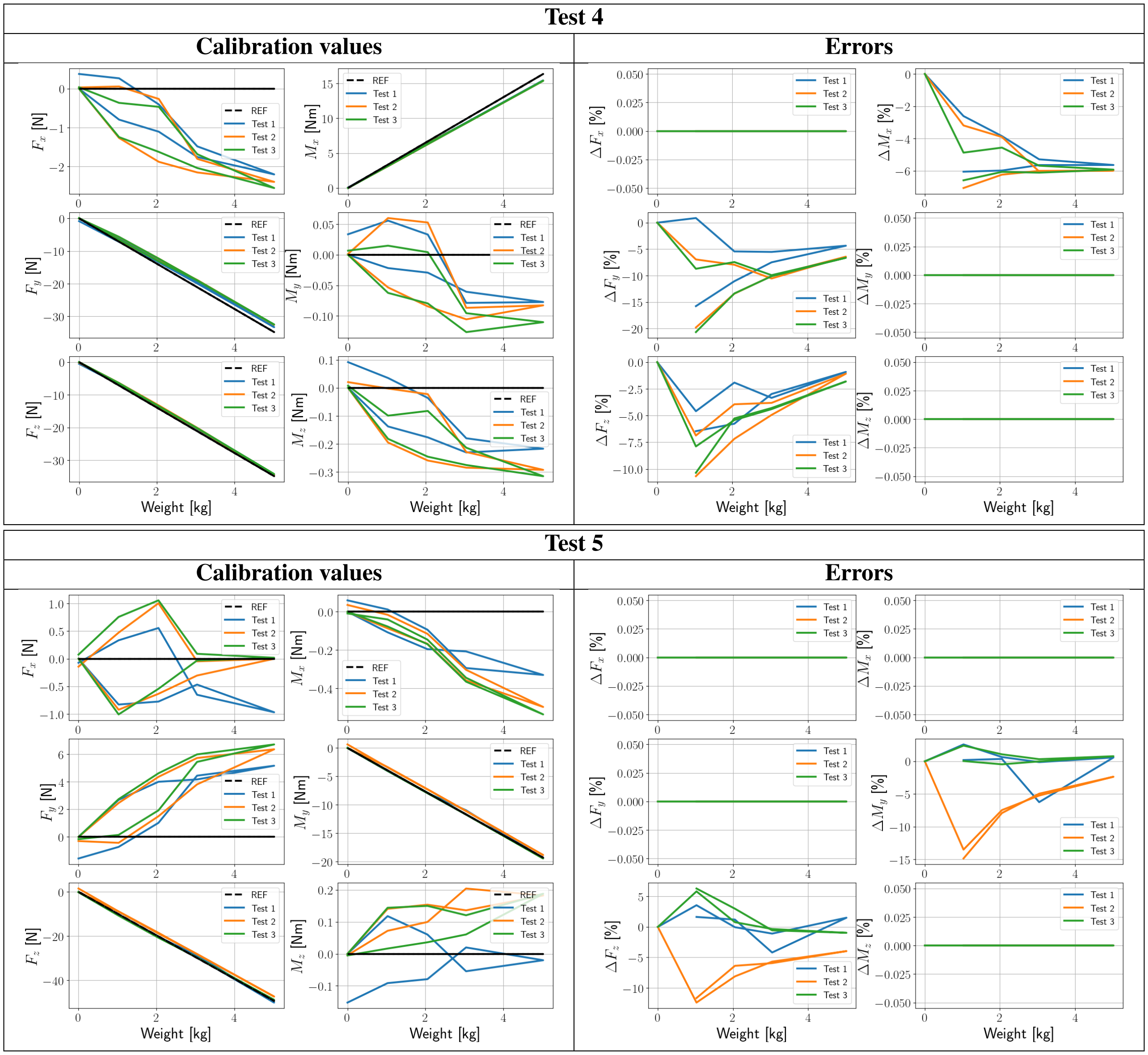

Table 4. Calibration and errors measured on the six axes for the five different tests.

ACKNOWLEDGMENTS

The authors thank the ENAC (for letting us using the Volière to conduct the experiments), Toulouse Métropole, Région Occitanie and BPI. The authors also thank Melvin Auguste-Virginie for the technical support.

REFERENCES

1. Chanetz, B., Délery, J., Gilliéron, P., Gnemmi, P., Gowree, E. R., and Perrier, P., "Measurement of Aerodynamic Forces and Moments," *Experimental Aerodynamics: An Introductory Guide*, Chapter 8, Springer International Publishing, Cham, 2020, pp. 183–198. DOI: 10.1007/978-3-030-35562-3_8.

2. Gojon, R., Jardin, T., and Parisot-Dupuis, H., "Experimental Investigation of Low Reynolds Number Rotor Noise," *The Journal of the Acoustical Society of America*, Vol. 149, No. 6, 2021, pp. 3813–3829. DOI: 10.1121/10.0005068.

3. Leishman, J. G., *Principles of Helicopter Aerodynamics*, Cambridge University Press, New York, NY, 2000.

4. Huber, H., and Polz, G., "Helicopter Performance Evaluation for Certification," *Proceedings of the Ninth European Rotorcraft Forum*, Stresa, Italy, Sept. 13–15, 1983, Associazione Industrie Aerospaziali, Associazione Italiana di Aeronautica ed Astronautica, Paper No. 26.

5. Johnson, W., *Helicopter Theory*, Princeton University Press, Princeton, NJ, 1980, pp. 808–813.

6. Grip, H. F., Johnson, W., Malpica, C., Scharf, D. P., Mandic, M., Young, L., Allan, B., Mettler, B., and San

Martin, M., “Flight Dynamics of a Mars Helicopter,” *Proceedings of the European Rotorcraft Forum (ERF)*, 2017.

7. Halley, D. H., “ABC Helicopter Stability, Control, and Vibration Evaluation on the Princeton Dynamic Model Track,” *Proceedings of the American Helicopter Society 29th Annual Forum*, Washington, DC, 1973.

8. NASA, “Wind Tunnel Evaluation of Sikorsky Bearingless Main Rotor,” NASA Ames Research Center, URL: https://rotorcraft.arc.nasa.gov/Research/Programs/tunnel_sikorsky.html.

9. Stewart, D., “A Platform with Six Degrees of Freedom,” *Proceedings of the Institution of Mechanical Engineers, Part I: Journal of Systems and Control Engineering*, Vol. 180, No. 15, 1965, pp. 371–386.

10. Dwarakanath, T. A., Dasgupta, B., and Mruthyunjaya, T. S., “Design and Development of a Stewart Platform Based Force-Torque Sensor,” *Mechatronics*, Vol. 11, No. 7, 2001, pp. 793–809. DOI: 10.1016/S0957-4158(00)00048-9.

11. Blank, J., and Deb, K., “pymoo: Multi-Objective Optimization in Python,” *IEEE Access*, Vol. 8, 2020, pp. 89497–89509.

12. Van Rossum, G., and Drake, F. L., *Python 3 Reference Manual*, CreateSpace, Scotts Valley, CA, 2009.

13. Oh, H. S., Kang, G., Kim, U., Seo, J. K., You, W. S., and Choi, H. R., “Force/Torque Sensor Calibration Method by Using Deep-Learning,” *2017 14th International Conference on Ubiquitous Robots and Ambient Intelligence (URAI)*, Jeju, Korea, June 28–July 1, 2017, IEEE, ISBN 978-1-5090-3056-9, DOI: 10.1109/URAI.2017.7992898.

14. Deters, R. W., Ananda, G. K., and Selig, M. S., “Reynolds Number Effects on the Performance of Ailerons and Spoilers,” *39th Aerospace Sciences Meeting and Exhibit*, Jan. 8–11, 2001, Reno, NV, American Institute of Aeronautics and Astronautics, Paper No. AIAA 2001-908, DOI: 10.2514/6.2001-908.